Spatial variations of snow surface temperature in mountainous areas: modelling and validation with remote sensing

03 February - 30 June 2020

Alvaro ROBLEDANO PEREZ

Master 2 Sciences de la Terre et des Planètes, Environnement

Parcours Atmosphère - Climat - Surfaces Continentales

Supervised by Ghislain PICARD & Laurent ARNAUD

Institut des Géosciences de l'Environnement (IGE)

Master Sciences de la Terre et des planètes, Environnement

Attestation de non plagiat

Je soussigné(e) (Prénom NOM)

Alvaro ROBLEDANO PEREZ

Auteur du mémoire (Titre)

Spatial variations of snow surface temperature in mountainous areas: modelling and validation with remote sensing

Déclare sur l'honneur que ce mémoire est le fruit d'un travail personnel et que je n'ai ni contrefait, ni falsifié, ni copié tout ou partie de l'œuvre d'autrui afin de la faire passer pour la mienne.
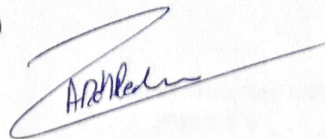
Toutes les sources d'information utilisées et les citations d'auteur ont été mentionnées conformément aux usages en vigueur.

Je suis conscient(e) que le fait de ne pas citer une source ou de ne pas la citer clairement et complètement est constitutif de plagiat, et que le plagiat est considéré comme une faute grave au sein de l'Université, pouvant être sévèrement sanctionnée par la loi.

Fait à Grenoble,

Le 19 | 06 | 2020

Signature de l'étudiant(e)

Remerciements

Impact of COVID-19

The COVID-19 pandemic has affected the measurement campaigns that were planned throughout March 2020. This prevent us to further explore one of the original objectives of this study: the adequacy of thermal cameras to represent the spatial variations of surface temperature in mountainous areas. Anyway, the subject of the study was revised and we obtained succesful results.

From an operational point of view, working from home has not been a positive experience. The apartment I live in is not really conceived to be used as a daily working place, with lack of suitable furniture and dedicated space. Home physical exercise and regular breaks were needed to prevent further physical harm.

Abstract

The temporal evolution of the snowpack is controlled by the surface temperature, which plays a key role in physical processes such as snowmelt. It shows large spatial variations in mountainous areas, where the illumination conditions are variable and depend on the topography. The surface energy budget is affected by the particular processes that occur in these areas, such as the modulation of the illumination by local slope and the re-illumination of the surface from surrounding slopes. These topography effects are often neglected in models, considering the surface as flat and smooth. Here we aim at estimating the snow surface temperature and its spatial variations in an alpine rugged terrain, in order to evaluate the role of the different processes that govern the variations of surface temperature. For this, a modelling chain is implemented to derive surface temperature from in-situ measurements. The main component is the rough surface ray-tracing (RSRT) model, based on a photon transport algorithm to quantify the impact of surface roughness in snow-covered areas. During this work, the surface scheme has been improved by considering the turbulent heat fluxes and the altitudinal variations of air temperature. To assess the performance of the model, we use in-situ measurements and satellite thermal observations (TIRS sensor aboard Landsat-8) in the Col du Lautaret area, in the French Alps. The satellite images are corrected from atmospheric effects with a single-channel algorithm. The results of the simulations show (i) an agreement between the simulated and observed surface temperature for a 30 h long time series in winter; (ii) the model bias (-0.23 °C and RMSE: 1.21 °C) at the in-situ measurement station is much less than the satellite observations bias (-1.98 °C and RMSE: 2.48 °C) ; (iii) the spatial variations of surface temperature are on the order of 5 to 10 °C between opposed slope orientations. The agreement with satellite observations is improved when considering topography effects, from $R^2 = 0.57$ to $R^2 = 0.75$ for a particular date on February 2018. A total of 20 Landsat-8 acquisitions have been considered, covering a wide variety of illumination conditions. Considering the importance of these processes in the surface energy budget, accounting for topography is therefore necessary to estimate the spatial variations of snow surface temperature.

Résumé

L'évolution temporelle du manteau neigeux est contrôlée par la température de surface. Elle montre une grande variabilité spatiale dans les zones de montagne, où les conditions d'illumination sont variables du fait de la topographie. Le bilan d'énergie de la surface est en effet affecté par les changements d'éclairement à cause de la pente locale et de l'orientation de la surface par rapport au soleil. Les modèles existants permettant de calculer la température de surface considèrent souvent la surface de neige comme lisse et horizontale. L'objective de cette étude est d'estimer la variabilité spatiale de la température de surface de la neige en terrain complexe, afin d'évaluer le rôle des differents processus qui influencent ces variations. Pour cela, une chaîne de modélisation a été implémentée avec en son coeur un modèle numérique de transport de photons (RSRT) récemment developpé. Pendant ce travail, le schéma de surface a été amélioré pour prendre en compte les flux de chaleur turbulents et le gradient altitudinal de la température de l'air. Pour évaluer la performance du modèle au Col du Lautaret, dans les Alpes, nous utilisons des mesures in situ et des observations satellitaires, issues du capteur TIRS sur Landsat-8. Les images satellite ont été corrigées pour prendre en compte l'atmosphère avec un algorithme du type single-channel afin d'estimer la température de surface. Les résultats des simulations montrent (i) un bon accord de l'estimation de la température de surface avec une série temporelle de mesures in-situ ; (ii) un faible biais entre les simulations et les données in-situ, et un biais modéré avec les observations satellite (-0.23 °C et -1.98 °C, respectivement) ; (iii) la variabilité spatiale de température de surface est de l'ordre de 5 à 10 °C entre des pentes opposées Nord et Sud. L'accord avec les observations est meilleur quand les effets liés à la topographie sont pris en compte, en particulier le rééclairement de la surface par des pentes voisines et la prise en compte du gradient altitudinal, le coefficient R^2 augmentant de 0.57 jusqu'à 0.75 pour une simulation en février 2018. 20 images Landsat-8 ont été considérées afin de couvrir une grande variété de conditions d'illumination. Prendre en compte la topographie apparait essentiel pour estimer avec précision la température de surface de la neige et sa variabilité spatiale.

Contents

1 Introduction

The cryosphere is an integral part of the Earth's climate system. Among its different frozen components, it includes snow-covered areas, that reflect more solar radiation than any other natural surfaces (Dozier et al., 2009). Snow is common both in polar and mountainous regions, and as it covers about a third of the Northern Hemisphere terrestrial surface during winter, it plays a significant role on Earth's surface energy budget (Imbrie and Imbrie, 1980; Flanner and Zender, 2005). Understanding the reflection and absorption of solar energy by snow is therefore important at many different spatial scales, as this controls the evolution of the snowpack, but also affects the hydrological cycle and avalanche risk forecasting (Flanner et al. 2007; Vionnet et al. 2012). Snow drives substantial changes to all energy fluxes that take place at the interface between the surface and the atmosphere. The surface energy budget is divided in two principal terms: the heat fluxes resulting from the turbulence in the boundary layer above the surface (sensible and latent heat fluxes), and the radiative fluxes (Male and Granger, 1981). The latter is split into the shortwave radiation (from $0.3\,\mu m$ to $5\,\mu m$) and the longwave radiation (from $5\,\mu m$ to $100\,\mu m$), and comprise the upwelling and downwelling contributions to the surface, upwelling meaning from the surface to the atmosphere, and downwelling meaning from the atmosphere to the surface. Both shortwave and longwave upwelling fluxes of the radiative balance depend on the nature of the surface: the longwave flux is driven by snow surface temperature (hereafter T_s), and shortwave flux is governed by the snow albedo, defined as the proportion of incoming shortwave radiation reflected by the surface. As it controls the quantity of solar energy absorbed by the snowpack, understanding the snow albedo variations is therefore essential.

Considering rugged terrain, the shortwave radiation received at the surface presents spatial variations. Small rough features (i.e. sastrugi) can potentially trap photons in their cavities, decreasing albedo and enhancing the absorption locally (Warren et al., 1998; L'Hermitte et al., 2014). Being θ_s the solar zenith angle (angle between the zenith and the incident solar angle), topography introduces a different local solar zenith angle, θ'_s, that depends on the surface's tilt. Shadowed areas do not receive direct radiation, but in turn they receive radiation reflected from surrounding slopes. The influence of the surface's tilt on the absorbed radiation is the main difference with respect to flat, smooth terrain. The local variations of snow albedo and absorption by the snowpack lead to differences on the radiative balance and therefore have an impact on snow surface temperature. Some efforts have been made to evaluate the longwave radiation in snow-covered areas (Marks and Dozier, 1979; Plüss and Ohmura, 1997). Lee et al. (2013) showed that the inclusion of topography effects have an impact on surface radiation budget over the Tibetan Plateau. While some physical and chemical properties of the snowpack, such as the Specific Surface Area (SSA – Grenfell and Warren, 1999) or the presence of light-absorbing impurities (Skiles et al., 2018), are considered in detailed snowpack evolution models (Carmagnola et

al., 2013; Tuzet et al., 2017), snow is usually represented as flat and smooth.

In addition to traditional in-situ measurements, surface temperature products from thermal satellite observations represent a good choice when evaluating the spatial variability of snow surface temperature. Remote sensing techniques have been widely used to monitor snow-covered surfaces on Earth. Optical satellite observations are mainly employed to derive information about the snow physical properties, as they are based on surface reflectance products (Mondet and Fily, 1999; Campagnolo et al., 2016). The observation in the thermal infrared (TIR) domain around (10.5 µm to 12.5 µm) wavelengths allows the retrieval of surface temperature. Even though several TIR bands are available from some missions, as the Advanced Spaceborne Thermal Emission and Reflection Radiometer (ASTER) onboard Terra satellite, or the Visible Infrared Imaging Radiometer Suite (VIIRS) onboard the Suomi National Polar-Orbiting Partnershipp (Suomi NPP) spacecraft, only Landsat missions have an archive of nearly 40 years of thermal imagery. The relatively high spatial resolution of their products (30 m) is adequate when considering spatial variations of surface temperature at the topography scale. From Landsat 4-5's Thematic Mapper to the most recent Thermal Infrared Sensor (TIRS) aboard Landsat-8, an enormous amount of thermal images are available to work with. Land Surface Temperature (LST) products have been mainly used for urban climate studies, drought monitoring and surface soil moisture estimation, among other fields (Li et al., 2013; Leng et al., 2016). However, remote sensing observations still find difficulties in mountainous areas. Both optical and thermal sensors suffer from changes on the surface illumination, i.e. different slopes and aspects (Sandmeier and Itten, 1997; He et al., 2019). This has motivated recent works in mountainous areas (Lamare et al., 2020) in the optical part of the spectrum, and there is a particular interest of the remote sensing community on the upcoming Landsat Level-2 Surface Temperature Science Product, courtesy of the United States Geological Survey (USGS – Web 1, last access: 19 June 2020).

This Master thesis aims at estimating the snow surface temperature in mountainous areas with a modelling chain that uses in-situ measurements. Thermal infrared observations are used in order to evaluate the spatial variations and the role of the different processes that take place in complex terrain. A 3D radiative transfer model developed at IGE (Institut des Géosciences de l'Environnement – Grenoble) by Ghislain Picard and Fanny Larue uses a Monte Carlo photon transport algorithm to quantify the impact of surface roughness in snow-covered areas. In the Rough Surface Ray Tracer (RSRT) model (Larue et al., 2020), a set of photons is sent to a surface described by a triangular mesh, i.e. a connected set of triangular facets, that can easily be derived from a Digital Elevation Model (DEM). The path of each individual photon is calculated, giving as a result the number of times a photon has hit each facet. A surface scheme uses subsequently this information to compute the shortwave and longwave radiation, and the surface temperature of each facet. This study is applied at the Col du

Lautaret area, in the French Alps. Section 2 provides a review of the basis of radiative transfer, the model description, as well as the method for retrieving LST from satellite images. Results are shown in Section 3, and discussed in Section 4. Final remarks and conclusion are addressed in Section 5.

2 Methods and materials

2.1 Surface energy budget

The surface temperature is determined by the surface energy budget. This budget comprises four different types of energy fluxes at a surface (Pal Arya, 1988): (i) the upwelling and downwelling radiation fluxes, whose algebraic sum is noted R_{net}; (ii) the sensible heat flux, noted H, that comes from the difference in temperature between the air and the surface; (iii) the latent heat flux, noted L, as a result of changes of state (evaporation, evapotranspiration or condensation) at the surface; and (iv) the ground heat flux, noted G, which is exchanged through the medium itself. The equation of the surface energy budget is therefore:

$$R_{net} + H + L + G = 0 \tag{1}$$

where all fluxes are expressed in $W\,m^{-2}$. R_{net} is split into the contributions of the shortwave radiation (from $0.3\,\mu m$ to $5\,\mu m$) and the longwave radiation (from $5\,\mu m$ to $100\,\mu m$), noted SW_{net} and LW_{net}, respectively. Each term corresponds to the balance between the downwelling radiation fluxes (SW_d and LW_d – from the Sun and atmosphere to the surface) and the upwelling radiation fluxes (SW_u and LW_u – from the surface to the atmosphere). The shortwave radiation fluxes are related via the broadband albedo, the proportion of incoming radiation reflected by the surface, noted α. Here, we consider snow as a blackbody in the longwave spectral range (emissivity = absorptivity = 1) , so the upward longwave radiation flux is determined by the Stefan-Boltzmann law:

$$LW_u = \sigma T_s^4 \tag{2}$$

being $\sigma = 5.67 \cdot 10^{-8}\,W\,m^{-2}\,K^{-4}$ the Stefan-Boltzmann constant, and T_s the snow surface temperature. The ground heat flux, G, is here neglected as the snowpack is considered thermalized, meaning that no energy is transferred downwards. Both the sensible and the latent heat fluxes are here considered following the simple approach used in the minimal snow model (MSM – Essery and Etchevers, 2004), and adapted by Picard et al. (2009) in their snow dynamic and emission model (SDEM):

$$H = \rho_{air}\, c_{p,air}\, C_H\, U\, (T_s - T_{air}) \tag{3}$$

$$L = L_s\, \rho_{air}\, C_H\, U \cdot (Q_{sat}(T_s, P_s) - Q_{air}) \tag{4}$$

where ρ_{air} and $c_{\text{p,air}}$ are the density and heat capacity of the air, U is the wind speed, T_{air} is the air temperature, $Q_{\text{sat}}(T_s, P_s)$ is the specific humidity at snow surface temperature T_s and pressure P_s, and C_H is a surface exchange coefficient. This coefficient depends on atmospheric stability. A detailed definition can be found on Picard et al. (2009). Here, for the sake of simplicity, a neutral situation is considered, so C_H stands for:

$$C_H = 0.16 \left[\ln(\frac{z_t}{z_0}) \ln(\frac{z_w}{z_0}) \right]^{-1} \tag{5}$$

Symbol	Description	Value
P_s	Air pressure	Altitude dependent
ρ_{air}	Air density	$P_s \cdot (287 \, T_{\text{air}})^{-1}$
$c_{\text{p,air}}$	Heat capacity of air	$1005 \text{ J kg}^{-1} \text{ K}^{-1}$
L_s	Sublimation heat	$2.838 \cdot 10^6 \text{ J·kg}^{-1}$
z_t	Temperature measurement height	3.53 m - snowdepth [m]
z_w	Wind speed measurement height	5.18 m - snowdepth [m]
z_0	Roughness length	10^{-3} m

TABLE 1 – Definitions and values of the symbols and magnitudes that are involved on the simplified calculation of turbulent fluxes.

Definitions of all symbols and their values can be found in Table 1. Some of them are based on in-situ measurements (Section 2.3). The equation of the surface energy budget for each facet of a modelled surface therefore remains:

$$SW_{\text{net, facet}} + LW_{\text{d, facet}} - \sigma T_s^4 + H_{\text{facet}} + L_{\text{facet}} = 0 \tag{6}$$

The incoming shortwave radiation flux has spectral dependence (as well as the albedo), so the notion of spectral irradiance is introduced hereafter. The spectral dependence of the downwelling longwave radiation flux is here neglected. The modelling chain implemented to estimate T_s is shown below.

2.2 Modelling chain

Figure 1 shows the general flowchart of the modelling chain to estimate snow surface temperature, T_s. TOM notation corresponds to "top-of-mountain", meaning on top of the studied location, and $facet$ notation corresponds to the surface. Several models (green boxes) are needed to simulate the different terms of the energy budget (orange boxes). All models, steps and the required inputs are described in the following sections.
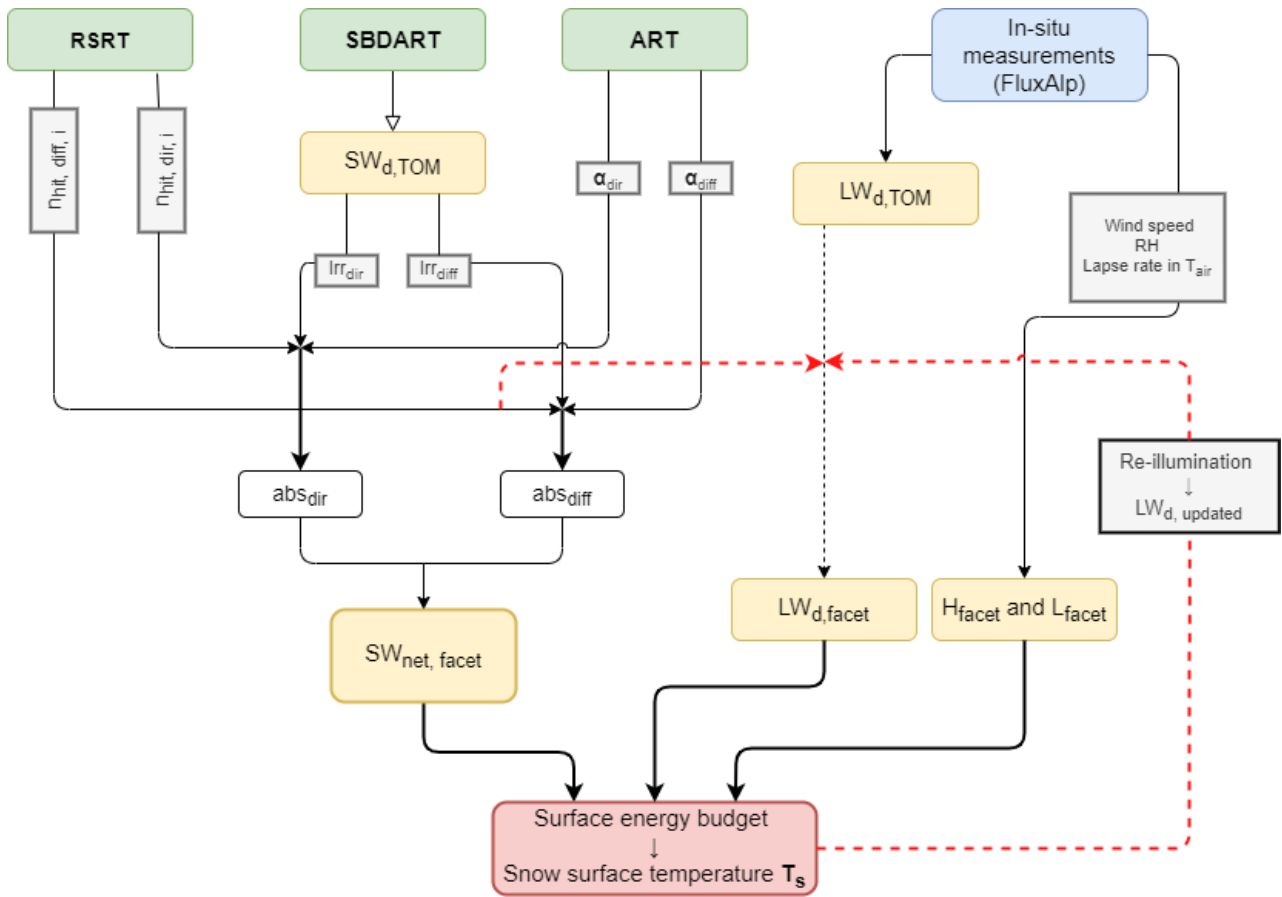
FIGURE 1 – Flowchart of the modelling chain to estimate snow surface temperature. The models involved are in green, and the terms of the surface energy budget are in orange. The red dashed lines indicate the last steps of the chain.

2.2.1 SBDART model

The direct solar spectral irradiance and the diffuse irradiance coming from the sky (noted: $SW_{d, TOM}$, and split into $Irr_{dir}(\lambda)$ and $Irr_{diff}(\lambda)$, respectively) are simulated with the Santa Barbara DISORT Atmospheric Radiative Transfer model (SBDART – Ricchiazzi et al., 1998), an atmospheric model that computes radiative transfer in both clear and cloudy conditions. It considers several atmospheric transmission models and the Mie theory to take scattering results into account. The simulations are run every 3 nm from 300 to 2000 nm, with the appropriate atmospheric and illumination conditions (atmospheric profile depending on location, no aerosol layer, solar zenith and azimuth angles corresponding to a particular date and time, etc).

2.2.2 Asymptotic Radiative Transfer theory

The intrinsic spectral albedo is computed using the Asymptotic Radiative Transfer (ART) theory. It allows estimating spectral albedo for highly reflective materials, such as snow (Kokhanovsky and Zege, 2004). Based on several assumptions about the snowpack (semi-infinite, vertical and horizontal homogeneous layers) and the surface (flat and smooth), both direct and diffuse components of the albedo

are expressed as follows:

$$\alpha_{\text{dir}}(\lambda, \theta_{\text{s}}) = \exp\left(-\frac{3}{7}(1 + 2\cos\theta_{\text{s}})\sqrt{a_\lambda}\right) \tag{7}$$

$$\alpha_{\text{diff}}(\lambda) = \exp\left(-\sqrt{a_\lambda}\right) \tag{8}$$

where a_λ a factor that depends on snow microstructure (SSA), the ice absorption coefficient and impurity content. SSA measurements are needed as input, and are taken from Tuzet et al. (2020) (Section 2.3). A Python library named Snowoptics has been developed to perform the calculations of snow albedo on flat and tilted terrains using the ART theory (Picard, 2020).

2.2.3 Rough Surface Ray Tracer model

The RSRT model computes the propagation path of a large number of photons launched towards a rough surface, until they escape from the scene. At the end of its path, each photon has hit the surface one or several times. The number of hits (and its order) is the key information to simulate the absorbed shortwave radiation by the snowpack.

The surface is represented by a mesh composed by triangular facets, given as an input. Here, the mesh used for simulations was built from the RGE ALTI®Version 2.0 Digital Elevation Model (DEM) provided by IGN France (Web 2, data available under conditions, last access: 19 June 2020). Data was acquired using radar techniques in mountainous areas as the Alps (i.e. the study area – Section 2.3) in 2009. The coordinate reference system is Lambert 93 (EPSG: 2154), and the original spatial resolution was of 5 m. It was resampled to 10 m due to computational limitations: the number of triangular facets was too high to perform simulations on a personal computer. Each photon has an initial intensity and a propagation direction $\vec{i}$, specified by the solar zenith and azimuth angles, also given as inputs. Edge effects are avoided by excluding the outermost 15% of the mesh from illumination.

An extended description of the algorithm is provided by Larue et al. (2020), here we recall the main steps: (1) estimation of the intersection between the photon path and the mesh (hereafter, a "hit"); (2) update the intensity: decrease by a factor (1 - albedo); (3) determination of the outgoing direction, and (4) update of the direction $\vec{i}$. The algorithm iterates until the photon escapes from the scene or its intensity is lower than a defined threshold (0.01, relative to the initial intensity that is equal to 1 – unitless quantities of energy). The facets here are considered as Lambertian – light is reflected equally in all directions, so the outgoing direction is randomly picked with a cosine-weighted hemispherical distribution.

The model counts the number of hits per facet, according to when, in its propagation path, a photon

has hit the facet (1st hit, 2nd hit, etc.). Noted $n_{hit,\,i}$, this number corresponds to the proportion of the total number of photons that hit the facet on their i^{th} hit. Two consecutive simulations are run, in both direct and diffuse illumination conditions. The results of the model ($n_{hit,dir,i}$ and $n_{hit,diff,i}$, respectively) are then incorporated to the modelling chain to estimate the net shortwave radiation per facet, $SW_{net,\,facet}$.

2.2.4 Snow surface temperature estimation

The estimation of snow surface temperature is done by solving the surface energy budget equation (Eq. 6). This is first carried out by assuming the surface is flat for the longwave radiation. Actually, in complex terrain, facets eventually see the re-illumination from surrounding facets. This is considered in the modelling chain by updating the downwelling longwave radiation flux (red dashed lines in Figure 1), and re-calculating T_s. Here we describe the steps followed to derive T_s in mountainous areas.

First, to simulate the absorbed shortwave radiation per facet, $SW_{net,\,facet}$, a spectral absorption coefficient is computed for both illumination conditions. It accounts for multiple reflection using the number of hits per facet, issued from the RSRT model:

$$\mathrm{abs}_{\mathrm{dir}}(\lambda, \theta_s) = (1 - \alpha_{\mathrm{dir}}(\lambda, \theta_s)) \sum_{i=0}^{i=n_{\max}} \alpha_{\mathrm{dir}}^i(\lambda, \theta_s)\, n_{\mathrm{hit,\,dir,\,i}} \tag{9}$$

$$\mathrm{abs}_{\mathrm{diff}}(\lambda) = (1 - \alpha_{\mathrm{diff}}(\lambda)) \sum_{i=0}^{i=n_{\max}} \alpha_{\mathrm{diff}}^i(\lambda)\, n_{\mathrm{hit,\,diff,\,i}} \tag{10}$$

The net broadband shortwave radiation is then calculated accounting for the incoming spectral irradiance (direct and diffuse), derived from SBDART model:

$$SW_{\mathrm{net,dir}}(\theta_s) = \int_{0.3\,\mu m}^{2\,\mu m} abs_{\mathrm{dir}}(\lambda, \theta_s)\, \mathrm{Irr}_{\mathrm{dir}}(\lambda)\, d\lambda \tag{11}$$

$$SW_{\mathrm{net,diff}} = \int_{0.3\,\mu m}^{2\,\mu m} abs_{\mathrm{diff}}(\lambda)\, \mathrm{Irr}_{\mathrm{diff}}(\lambda)\, d\lambda \tag{12}$$

$$SW_{\mathrm{net}}(\theta_s) = SW_{\mathrm{net,dir}}(\theta_s) + SW_{\mathrm{net,diff}} \tag{13}$$

Second, the downwelling longwave radiation flux, $LW_{d,\,facet}$ is obtained from in-situ measurements (FluxAlp – Section 2.3) and is considered constant over the whole scene. The turbulent fluxes (H_{facet} and L_{facet}) are also simulated from in-situ measurements with the simple approach proposed by Picard et al. (2009) (Eqs. 3 and 4). Here, to account for the differences in altitude between the facets in the

mesh, a lapse rate effect for the air temperature is introduced:

$$T_{\text{air,facet}} = T_{\text{air, obs}} + \Gamma \left(z_{\text{facet}} - z_{\text{obs}}\right) \tag{14}$$

where $\Gamma = -6\,°\text{C km}^{-1}$ is a constant lapse rate value across the scene. Only air temperature is considered to depend on altitude, while wind speed and relative humidity are considered constant.

The surface energy budget equation for each facet is then to be solved for T_s. It is a nonlinear equation, with the upwelling longwave radiation flux , $LW_{\text{u, facet}}$ dependent on T_s^4, the sensible heat flux term dependent on T_s and the latent heat flux dependent T_s in a complex way through the humidity. This last term is linearized to present the surface energy budget equation as a simplified quartic equation for T_s:

$$\text{a } T_s^4 + \text{d } T_s + \text{e} = 0 \tag{15}$$

To account for the fact that each facet in rugged terrain "sees" the sky as a majority, but is also re-illuminated from the surrounding facets, the sky-view factor is introduced, noted V. The surrounding facets emit longwave radiation for its own T_s, as stated by the Stefan-Boltzmann law (Eq. 2). It is represented in the modelling chain as the proportion of photons hitting a facet on at the first bounce in diffuse illumination (so i = 1). Here an important approximation is done, by considering the re-illumination constant for all of the facets. It means that they all emit the same average longwave radiation based on the T_s of each facet, $LW_{\text{u, mean}}$. The $LW_{\text{d, facet}}$ term is updated as follows:

$$LW_{\text{d, facet, updated}} = V \; LW_{\text{d, TOM}} + (1 - V) \; LW_{\text{u,mean}} \tag{16}$$

T_s is estimated for each facet of the simulated surface by solving the quartic equation again, considering the updated longwave term. This last part of the chain is represented in Figure 1 by the red dashed lines.

2.3 Study area

Figure 2 shows the extent of the study area. It is located around the Col du Lautaret, a mountain pass located at 2057 m a.s.l. in the French Alps (45.0°N, 6.4°E). This area is interesting for surface temperature, as it covers both north and south-facing slopes, in addition to smaller-scale rugged terrain covering the rest of orientations. The size of the area has been defined considering the computational limitations of a personal computer, while covering a large diversity of rough features. The study area is also well-instrumented, with the measurement station FluxAlp located within a few hundred meters, on the *Pré des Charmasses* site. This site collects meteorological and radiometric observations since
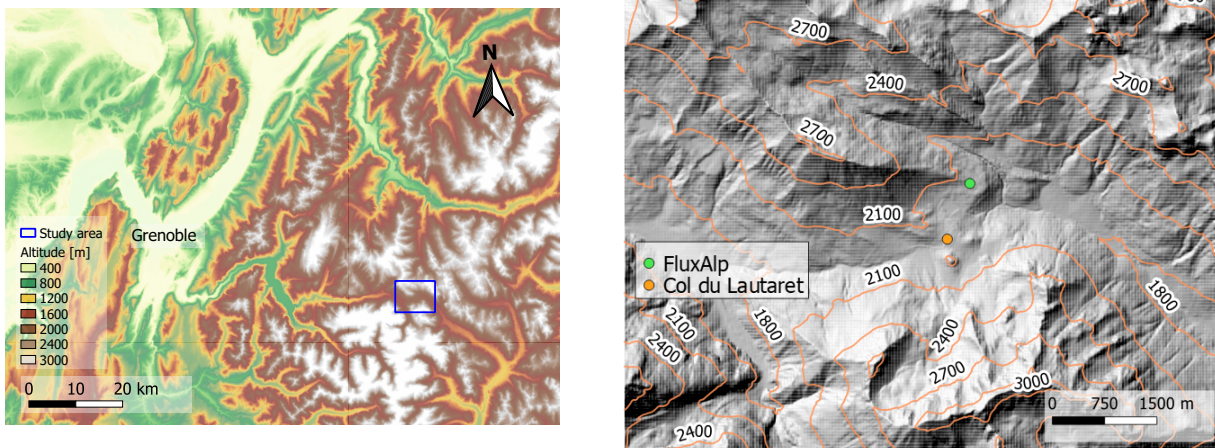
FIGURE 2 – Location of the study area, around the Col du Lautaret alpine site. The blue rectangle on the left side represents the hillshade product on the right side. This product is generated from the RGE ALTI®Version 2.0 Digital Elevation Model (DEM) provided by IGN France, with a spatial resolution of 10 m.

October 2012 (Choler et al., 2014), and several snow measurement campaigns have taken place at this site in the past (Dumont et al., 2017; Larue et al., 2020). Radiation fluxes are measured with a Kipp & Zonen CNR4 net radiometer, and averaged as the other variables over 30 minutes. When deriving surface temperature from radiometric observations, an uncertainty of 1 K is estimated. The data needed as input for the modelling chain is issued from here (meteorological – air temperature, wind speed, relative humidity and radiometric – downwelling longwave radiation flux). SSA measurements for two consecutive winter seasons (2016 / 2017 and 2017 / 2018) have been provided by Tuzet et al. (2020). The measurements were collected with the DUFISSS instrument (DUal Frequency Integrating Sphere for Snow SSA measurement, Gallet et al., 2009) during the first season, and with the Alpine Snowpack Specific Surface Area Profiler (ASSSAP, a lighter version of POSSSUM instrument, described in Arnaud et al., 2011) during the second season. These measurements have an estimated uncertainty of 10 %.

In order to evaluate the model, FluxAlp data is insufficient as it is only based in a single point. A spatially-distributed surface temperature dataset is described in the following sections.

2.4   Surface temperature retrieval with Landsat-8 observations

Spatial variations of surface temperature are retrieved from satellite observations. The two thermal bands (TIRS – Band 10 and Band 11) aboard Landsat-8 cover the spectrum between 10.6 µm to 12.51 µm, with a spatial resolution of 100 m (resampled by Cubic Convolution methods to 30 m) and a 16 day repeat cycle. Only Level-2 data from the optical sensor is publicly available outside the United States, meaning that thermal observations are only provided as Top-Of-Atmosphere radiances. Different methods to correct atmospheric effects have been implemented to retrieve Land Surface Temperature (LST, hereafter). These methods are based on split-window methods (Jin et al., 2015), mono-

window techniques (Tardy et al., 2016), or a single-channel approach (Jiménez-Muñoz and Sobrino, 2003). An excellent review is provided by Li et al. (2013). Soon after the launch of Landsat-8, stray light was observed on thermal data (Montanaro et al., 2014), coming from scattering of outer radiance. A nonuniform signal is observed, affecting mainly the Band 11. USGS still recommends not to use Band 11 for the split-window technique. Only recently (Web 3, last access: 19 June 2020), calibration parameters have been adjusted and data of the upcoming Collection 2 (during 2020) will benefit from this correction. Methods based on only one band are therefore suggested, considering the mean atmospheric temperature and the atmospheric transmittance as an input on radiative transfer codes (i.e., MODTRAN). Figure 3 shows the flowchart to retrieve LST from satellite observations, as proposed by Cristóbal et al. (2018):
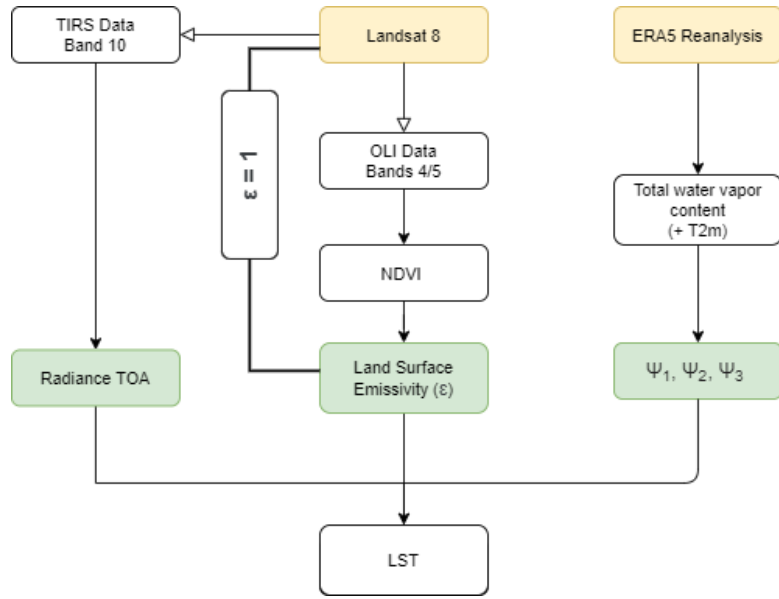

FIGURE 3 – Workflow to retrieve Land Surface Temperature from Landsat-8 thermal observations with a single-channel approach.

The single-channel algorithm is the most suitable method when no in-situ radiosonde data is available, or access to radiative transfer codes is difficult. The approach of the algorithm consists in approximating the atmospheric functions from atmospheric water vapor content (w, in $\mathrm{g\,cm^{-2}}$). Cristóbal et al. (2018) presented an improved single-channel method dependent not only on water vapor content, but also on near-surface air temperature (T_a), which are available from reanalysis data. Both the single-channel method (SC method – Jiménez-Muñoz and Sobrino, 2003) and the improved single-channel method (iSC method – Cristóbal et al. (2018)) have been implemented here, in order to determine which one is more accurate in the study area. LST is calculated by applying the radiative transfer equation to a sensor channel:

$$LST = \gamma \cdot \left[\varepsilon^{-1} \left(\psi_1 \cdot L_{\mathrm{sensor},\lambda} + \psi_2 \right) + \psi_3 \right] + \delta \tag{17}$$

where

$$\gamma = \left\{ \frac{c_2 \cdot L_{\text{sensor},\lambda}}{T_{\text{sensor}}^2} \left[\frac{\lambda^4}{c_1} L_{\text{sensor},\lambda} + \lambda^{-1} \right] \right\}^{-1} \tag{18}$$

$$\delta = -\gamma \cdot L_{\text{sensor},\lambda} + T_{\text{sensor}} \tag{19}$$

$$T_{\text{sensor}} = \frac{K_2}{ln \left(\frac{K_1}{L_\lambda} + 1 \right)} \tag{20}$$

where ε is the emissivity of the pixel, ψ_i are the atmospheric functions that are parameterized, λ is the effective wavelength (10.904 µm for Band 10), $L_{\text{sensor},\lambda}$ is the top of atmosphere radiance calculated from pixel Digital Numbers (DN) using rescaling factors (Web 4, last access: 19 June 2020), and T_{sensor} is the brightness temperature (in K). Values and symbols can be found in Table 2.

Symbol	Unity	Value
c_1	W µm^4 m^{-2} sr^{-1}	$1.19104 \cdot 10^8$
c_2	µm K	$1.43877 \cdot 10^4$
K_1	W m^{-2} sr^{-1} µm^{-1}	774.89
K_2	K	1321.08

TABLE 2 – Definitions of symbols involved on LST retrieval.

The atmospheric functions are statistically fitted from the GAPRI database (Mattar et al., 2015): 4714 atmospheric profiles covering from tropical to arctic atmospheric conditions. The following fit is applied here:

$$\psi_i = i \, w^2 + h \, T_{\text{a}}^2 + g \, w + f \, T_{\text{a}} + e \, T_{\text{a}}^2 \, w + d \, T_{\text{a}} \, w + c \, T_{\text{a}} \, w^2 + b \, T_{\text{a}}^2 \, w^2 + a \tag{21}$$

All the coefficient values (from i to a) can be found in Cristóbal et al. (2018). Here the emissivity is considered equal to 1 on the whole scene is made, so as to be consistent with Eq. 2. Water vapor and near-surface air temperature data comes from ERA5 Reanalysis dataset (C3S, 2017). They are taken from the closest grid reanalysis point to the scene. In order to cover a large range of solar zenith angles, a total of 20 cloudless thermal images from different winter dates were selected, from February 2015 to December 2019. Unfortunately, during the two winter seasons that are covered by the work of Tuzet et al. (2020), only 4 of the Landsat-8 acquisitions correspond to their in-situ SSA measurements, in particular: 2, 18 and 27 February 2018, and 22 March 2018. The list of selected scenes can be found in the appendix.

2.5   Thermal infrared camera

Thermal infrared (TIR) imagery is an increasingly popular tool to measure surface temperature. TIR cameras measure radiation in the 8-14 µm domain and their size and light-weight allow them to be carried by unmanned aerial vehicles (UAVs), which can provide high resolution and spatially-resolved surface temperature data. This technique combines the advantages of in-situ measurements (possible high temporal resolution) and those of remote sensing techniques. These UAV-borne cameras imply a huge improvement in spatial resolution over typical satellite thermal measurements (centimeter vs 100 m from the Landsat-8 TIRS). Glaciologists have widely exploited the visible and near-infrared domains to track rapid changes or dynamics of glaciers (Rossini et al., 2018), with photogrammetry techniques such as structure-from-motion (SfM) to create orthophotos and Digital Surface Models. Such devices have also been used to map snow depth over different types of terrain. Bühler et al. (2016) showed the potential and limitations of such measurements, which are a crucial input for applications in hydrology, climatology or avalanche research. Until now, UAV-based thermal infrared imagery has been widely exploited for agricultural applications, such as monitoring crop water stress (Gomez-Candon et al., 2016) or evapotranspiration mapping (Brenner et al., 2017). TIR imagery has not been used as much for cryospheric applications. It has been mainly applied to derive surface temperature on debris-covered glaciers (Aubry-Wake et al., 2015; Kraaijenbrink et al., 2018), in order to better evaluate the glacier's surface energy budget.

All these previous works show the potential of TIR cameras to derive surface temperature. Nevertheless, accurate results are rarely obtained. This can be explained by the fact that these platforms need to mount light and uncooled thermal cameras. Their microbolometer is not stabilized at a constant temperature, so the fluctuations of the sensor and the camera body temperature impact the measure. Correction and calibration need to be done, such as proposed by Budzier and Gerlach (2015): (i) Non-uniformity correction, which smooths out the differences between individual pixels of the microbolometer; (ii) shutter correction, required due to the radiance emitted by the camera itself, that also varies with temperature. This correction, known as Flat Field Correction (FFC), is implemented by the manufacturer in the firmware based on time or changes in sensor temperature; (iii) radiometric calibration, by establishing the relationship between the response of the sensor and the absolute temperature of the image.

During this study, we planned to acquire both UAV-based and ground-based (time series via time-lapse photography) thermal images to validate the estimation of snow surface temperature, T_s. Before performing UAV-based measurements, calibration tests were undertaken in order to evaluate the precision and accuracy on snow of the camera, a Tau 2 640, from FLIR Systems. The sensor resolution is

of 640 x 512 pixels, and the camera is mounted with a 13 mm lens that offers a 45° x 37° field of view. The detector of the infrared radiation is an uncooled microbolometer, working in the spectral range of 7.5 - 13.5 μm. The acquisition rate is 8.33 Hz, and the image recording can be modified to the required time-lapse frequency. One calibration test was done on 7 March 2020 at the Col du Lautaret alpine site, during a clear-sky morning and under stable conditions. A snow surface was prepared and the camera was fixed for nearly 90 min to acquire a time series (2 min time-lapse frequency). The validation was performed at the same time with two Infrared Remote temperature sensors (IR120) from Campbell Scientific, that were pointed to two different areas within the TIR camera field of view. The uncertainty related to the temperature measurement is about 0.2 K under laboratory conditions, according to the manufacturer (Web 5, last access: 19 June 2020).

Unfortunately, the lockdown because of the COVID-19 pandemic has impeded further measurement campaigns, in particular UAV-based ones, which would have been worthwhile to this study.

3 Results

In order to validate the T_s estimation, the spatially-resolved observations are evaluated. First, TIR imagery and observations from Landsat-8 satellite are assessed, before the evaluation and validation of the model against the observations.
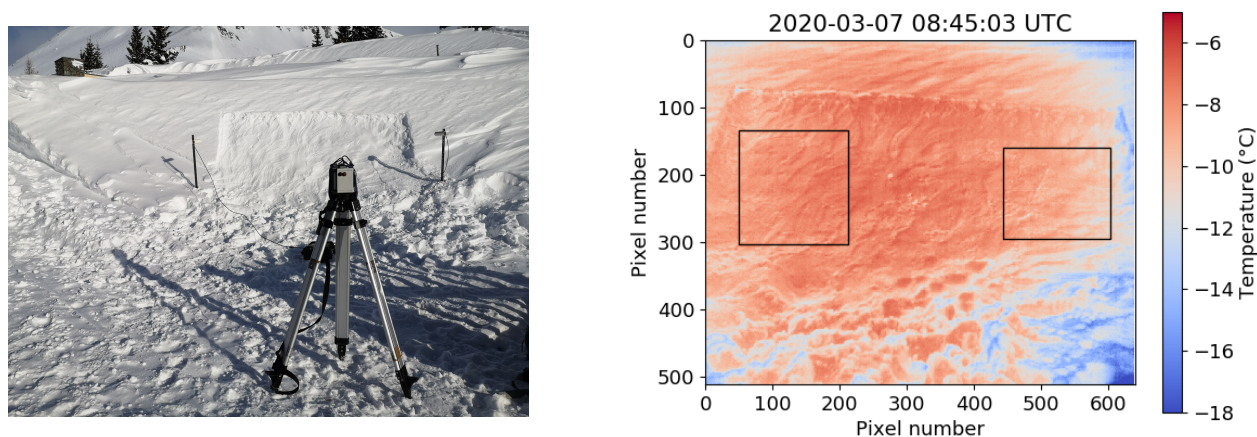
3.1 Thermal camera measurements

FIGURE 4 – On the left, photograph from the set up to calibrate the thermal (TIR) camera. On the right, non-calibrated image from the TIR camera. Both rectangles represent the zones where calibration is based on.

The calibration experiment was performed in presence of snow. Figure 4 shows, on the left, a photograph of the set up, with the TIR camera in the middle and the two surface temperature sensors (IR120) pointing to the outermost parts of the surface. It was prepared to be at a quasi-uniform tem-

perature (small area, uniform slope and orientation), so calibration could be easily performed. On the right, a non-calibrated image acquired with the camera shows the high variability of surface temperature measurements. A vignetting effect is visible close to the lower right corner. This is observed in the majority of the images taken by the TIR camera, as well as large temperature changes between consecutive acquisitions (10 to 15 °C variations).

To evaluate the fluctuations on the measurements, Figure 5 shows the temporal evolution of the temperature difference: (i) between the two surface temperature sensors (IR120 radiometers) and the TIR camera (FLIR), left and right (blue and red lines, respectively) zones corresponding to the rectangles in Figure 4; and (ii) between the inner parts of the TIR camera (green line).
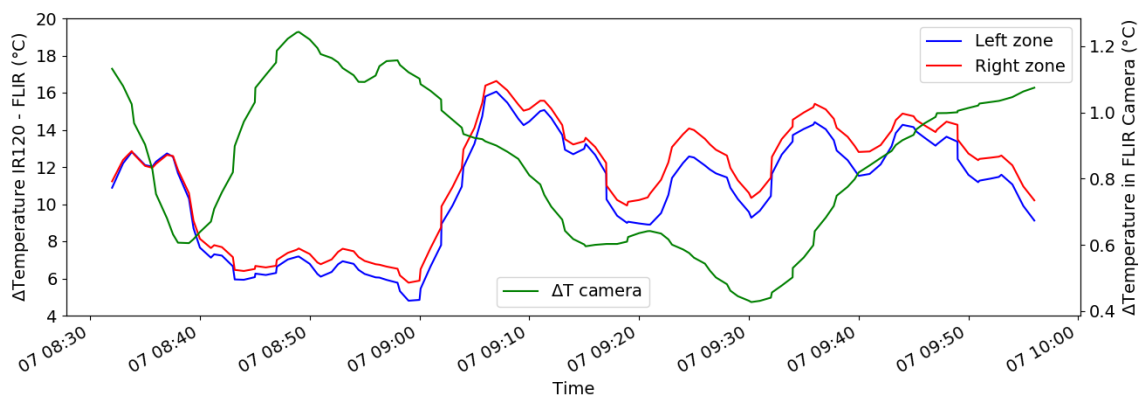

FIGURE 5 – Temperature differences between the IR120 radiometers and the thermal camera (red and blue lines) and between the inner parts of the thermal camera (green line).

The thermal camera measurements are in the range 5 to 15 °C off the reference temperature measured by the IR120 radiometers, and this seems to be correlated to the temperature difference between the inside parts. Other tests under varying conditions (ventilation, in particular) indicate the same correlation. This highlights the importance of a better understanding on how the camera calibrates itself to compensate these inner temperature changes. Unfortunately, lockdown because of COVID-19 pandemic prevented us to further explore this issue, essential for UAV-borne measurements.

3.2   Surface temperature observations with Landsat-8

The surface temperature observations from Landsat-8 (LST) are compared to FluxAlp measurements in order to evaluate the accuracy. The atmospheric correction is carried out by means of both the single-channel method (SC method) and the improved single-channel method (iSC method), to determine which one is more robust in the Col du Lautaret site. Figure 6 shows the surface temperature obtained by the retrieval methods as a function of the in-situ measurements. Values from Landsat-8 acquisitions are taken from the pixel covering the location of FluxAlp. The bias of the iSC method is smaller
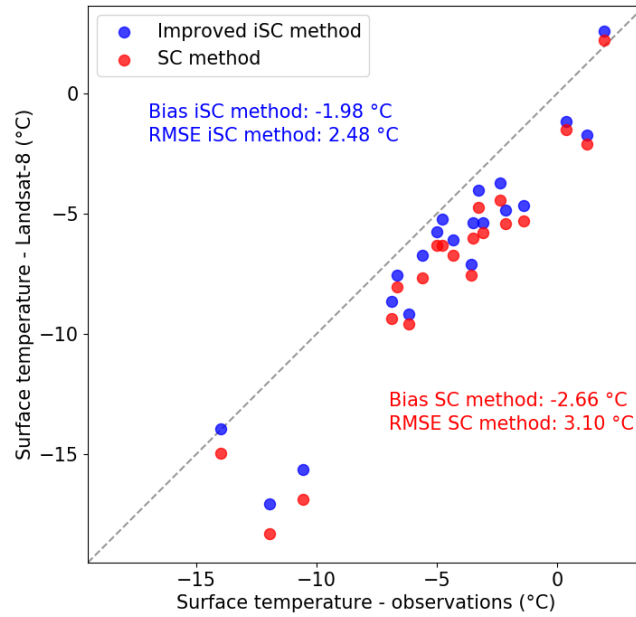
FIGURE 6 – Surface temperature estimated with Landsat-8 observations as a function of surface temperature measurements at FluxAlp site. Blue markers represent the improved iSC retrieval method while red markers represent the SC method. The 1:1 dashed line represents perfect agreement with observations.

than the one of the SC method (-1.9 °C and -2.6 °C, respectively). The bias is generally more important when considering cold conditions, between -10 °C and -15 °C, being the improved method (iSC) constantly warmer than the original method (SC). Without considering the two acquisitions where the underestimation is larger (around 5 °C on 2 February 2018 and on 29 January 2019), the bias is -1.6 °C (RMSE: 1.9 °C). Here, as an approximation, acquisition time of Landsat-8 observations (10h17 or 10h23 UTC depending on the scene) and measurements (10h30 UTC) are considered equal, as FluxAlp measurements are averaged over 30 min. The lack of real-time measurements can hide a bias on the T_s measurements, so this needs to be considered when assessing the accuracy of the method, as well as the own estimated accuracy at FluxAlp, around 1 °C. The improved single-channel method shows more accurate results, and it has been used here to evaluate the estimation of snow surface temperature.

3.3 Snow surface temperature estimation

3.3.1 Evaluation of the diurnal cycle dynamics

The modelling chain to estimate T_s variations is first evaluated over a diurnal cycle, before assessing its performance on spatial variability. A 30 h long time series was selected close to one of the Landsat-8 acquisition dates, starting at noon on 10 March 2016. This period featured stable conditions and the sky was clear, except few minutes at the end of the time series. The terms of the surface energy budget are simulated and compared to the in-situ measurements at FluxAlp site. Figure 7 (top) shows the temporal evolution of the radiative fluxes (SW_{net} and LW_{net}) and the turbulent fluxes (sensible heat flux H
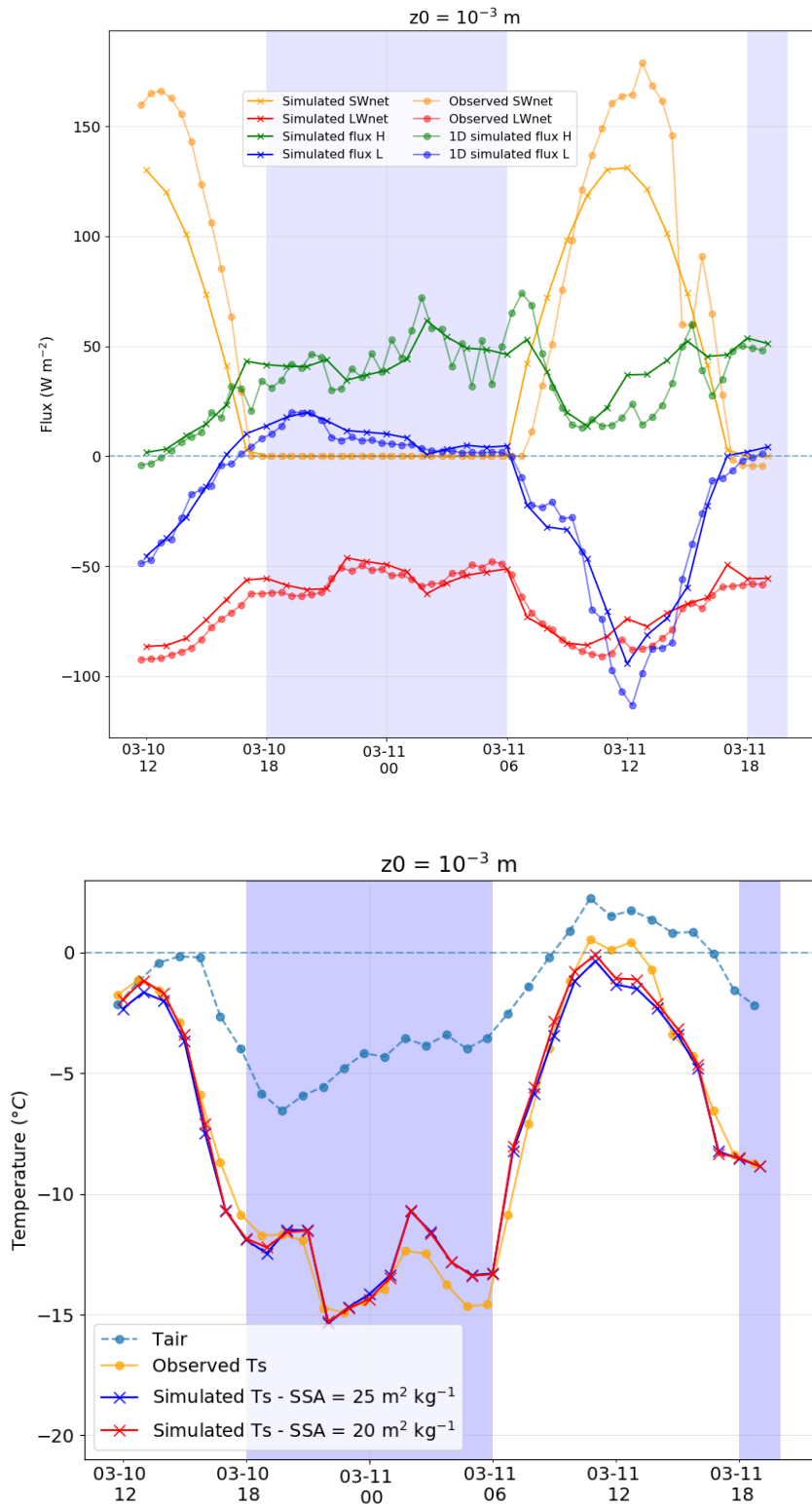
FIGURE 7 – Simulation of a 30 h long time series on March 2016. The terms of the surface energy budget (top) and snow surface temperature (bottom) are estimated at the FluxAlp measurement station to be compared to in-situ observations. The shadowed areas correspond to night time (i.e. $SW_{net} = 0\,W\,m^{-2}$). All times are in UTC.

and latent heat flux L). The simulations are run on an hourly basis, with constant SSA = $20\,m^2\,kg^{-1}$ and aerodynamic roughness length z0 = $10^{-3}\,m$. As measurements at FluxAlp station are averaged

over 30 minutes, a 15 min time shift is applied for a fair comparison. The results show that, while the net longwave flux is well estimated, the net shortwave flux is less accurate. This flux is overestimated during the first hours of sunlight, and underestimated during the rest of the day. This absorption bias is not significant around 10h-10h30 UTC, corresponding to the Landsat-8 acquisition time. The turbulent fluxes are well simulated compared to the values estimated from the observed wind speed, air temperature and humidity (from that the notation: 1D simulated). They use the same equations (Eq. 3 and Eq. 4) as for the simulated terms. Figure 7 (bottom) shows the evolution of the simulated T_s over the same period, compared to measurements. Two simulations are shown, with SSA values of 20 and 25 m^2 kg^{-1}, respectively. Observed air temperature (T_{air}) is also shown for completeness. There is an excellent agreement between the simulations and the measurements. The overestimation and underestimation of the net shortwave flux (and therefore the energy absorbed in the snowpack) could explain the bias of snow surface temperature in the morning and at the end of the afternoon.

In addition, Figure 8 shows observations by Landsat-8 and simulations by the model of snow surface temperature, compared to the in-situ observations. The bias of the model is only -0.2 °C (RMSE: 1.2 °C), much less than the satellite observations bias. The estimation of T_s at a particular point is accomplished for a large variety of illumination conditions (i.e. different solar zenith and azimuth angles).

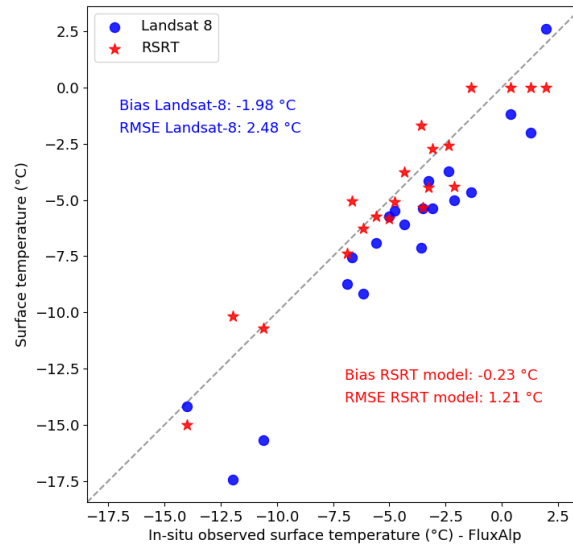FIGURE 8 – Comparison of simulated T_s by the model and observed T_s by Landsat-8 to in-situ measurements at FluxAlp site. All 20 Landsat-8 scenes are considered.

3.3.2 Evaluation of the spatial variations

To evaluate the spatial variations of T_s, the results here correspond to two of the Landsat-8 acquisition dates: 18 and 27 February 2018, respectively. These are chosen as SSA in-situ measurements are

available from Tuzet et al. (2020). The corresponding values are 45 and 53 $m^2 \, kg^{-1}$. The other results are shown in the appendix for completeness.
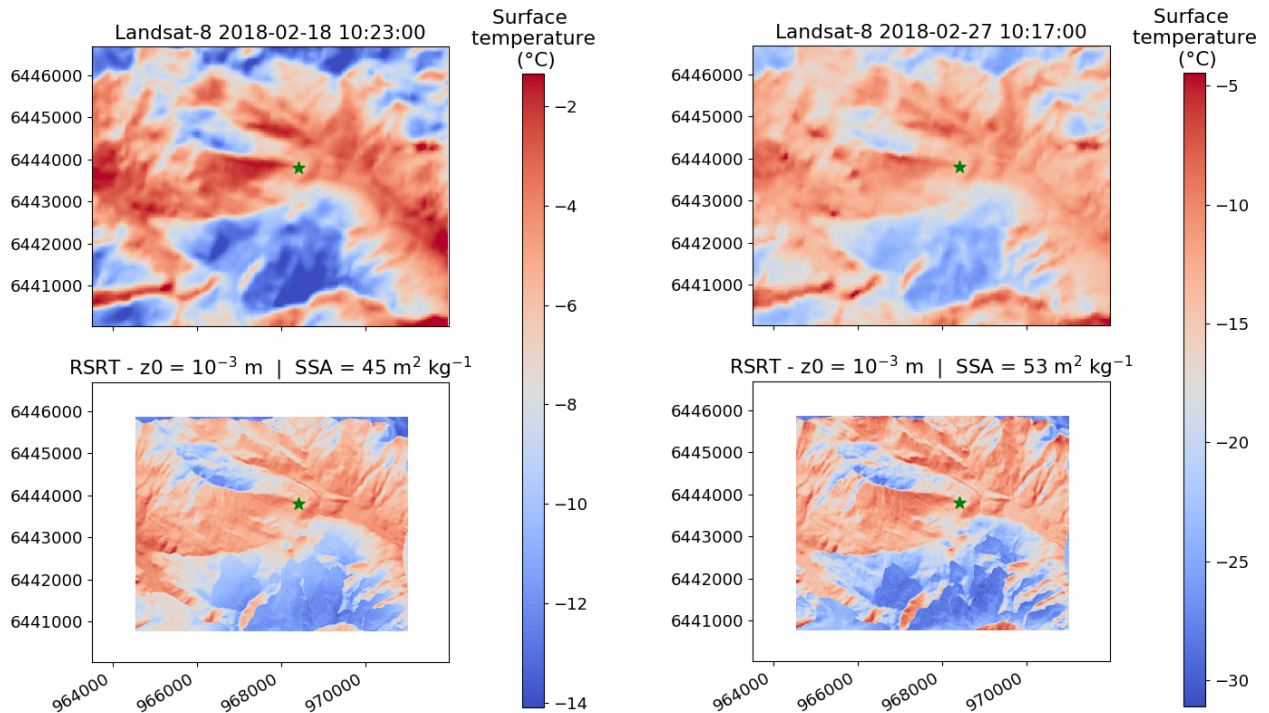

FIGURE 9 – Surface temperature maps, observed by Landsat-8 and estimated by the RSRT model, for two dates: 18 February 2018 (left) and 27 February 2018 (right). The location in the scene of the FluxAlp measurement station is highlighted by the green marker. Projection is Lambert 93 (EPSG: 2154) and the coordinates are in meters.

Figure 9 shows the spatial variations of the snow surface temperature, observed by Landsat-8 (top) and simulated by the modelling chain (bottom). The zone without data (white) in simulated images corresponds to the part of the mesh that is not illuminated to avoid edge effects. The variations are well represented by the model, with many similarities at all the scales across the images. The surface temperature is clearly dependent on topography, and in particular on slope orientation, showing large temperature gradients. Figure 10 shows the distribution of simulated T_s with respect to the aspect of the terrain. The gradient is large between opposite slopes, with lower surface temperatures in the shadowed, north-east facing areas at the south of the scene and warmer temperatures in the south-west facing areas around FluxAlp.

To highlight the effect of considering altitudinal variations of air temperature, Figure 11 displays the distribution of surface temperature for both dates, observed by Landsat-8 and simulated by the model (with and without the lapse rate). Introducing the lapse rate effect decreases the surface temperature, as the reference site (FluxAlp) is rather in the lower range of altitudes of the study area. This improves the agreement with the observations by satellite, in particular the case in Figure 11a, where the distribution shape is considerably widened. Figure 12 shows the scatterplots between observations and simulations on 18 February 2018 and 27 February 2018. The particular processes that take place
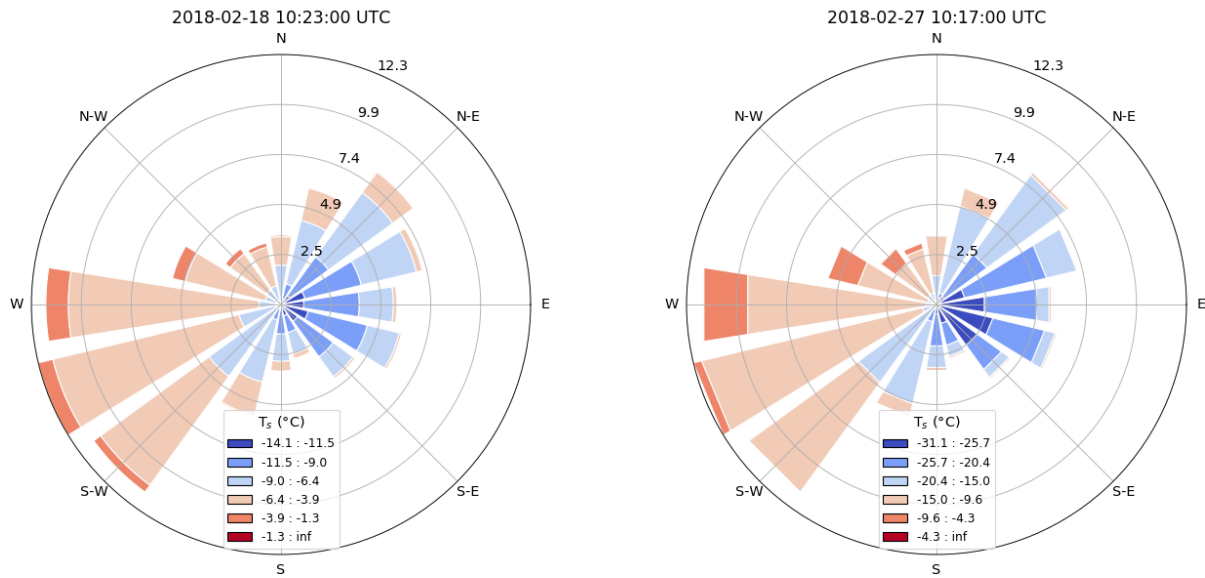
FIGURE 10 – Distribution of simulated surface temperature as a function of the aspect. The results are normed and displayed in percent.
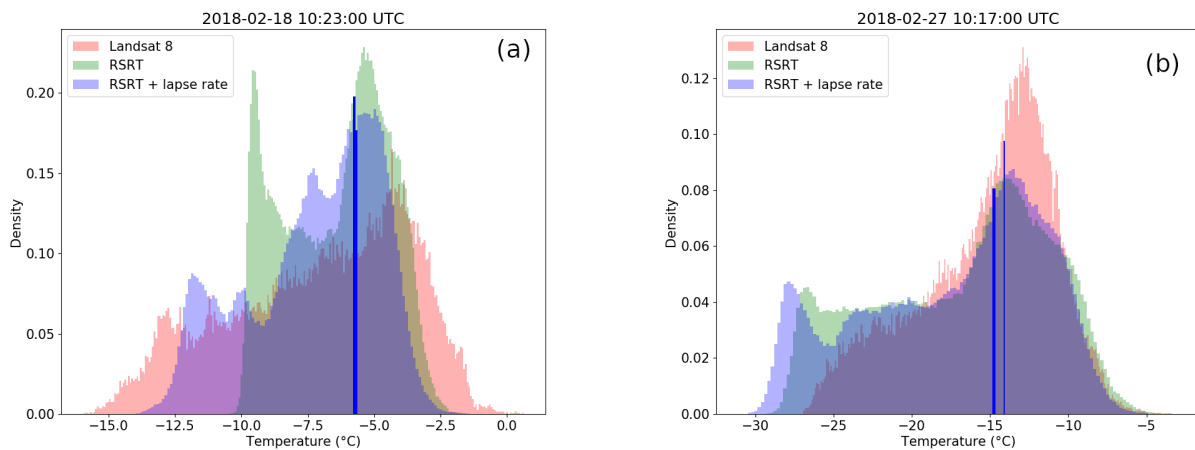

FIGURE 11 – Distribution of surface temperature from observations and simulations (with or without lapse rate effect for air temperature). The value corresponding to FluxAlp is highlighted with an intense blue rectangle. (a) corresponds to Landsat-8 acquisition from 18 February 2018, and (b) from 27 February 2018.

in rugged terrain are considered: without re-illumination by surrounding slopes (left); accounting for re-illumination (center); and introduction of a lapse rate in air temperature (right). In any cases, the local slope and the shadow are taken into account. The agreement with observations increases as these processes are considered (R^2 changes from 0.57 to 0.75 and from 0.61 to 0.71, for the two dates).

4   Discussion

Two main questions are discussed. The estimation of T_s and the spatial variations is first assessed (Section 4.1), and secondly, the limitations of the methods are discussed in Section 4.2.
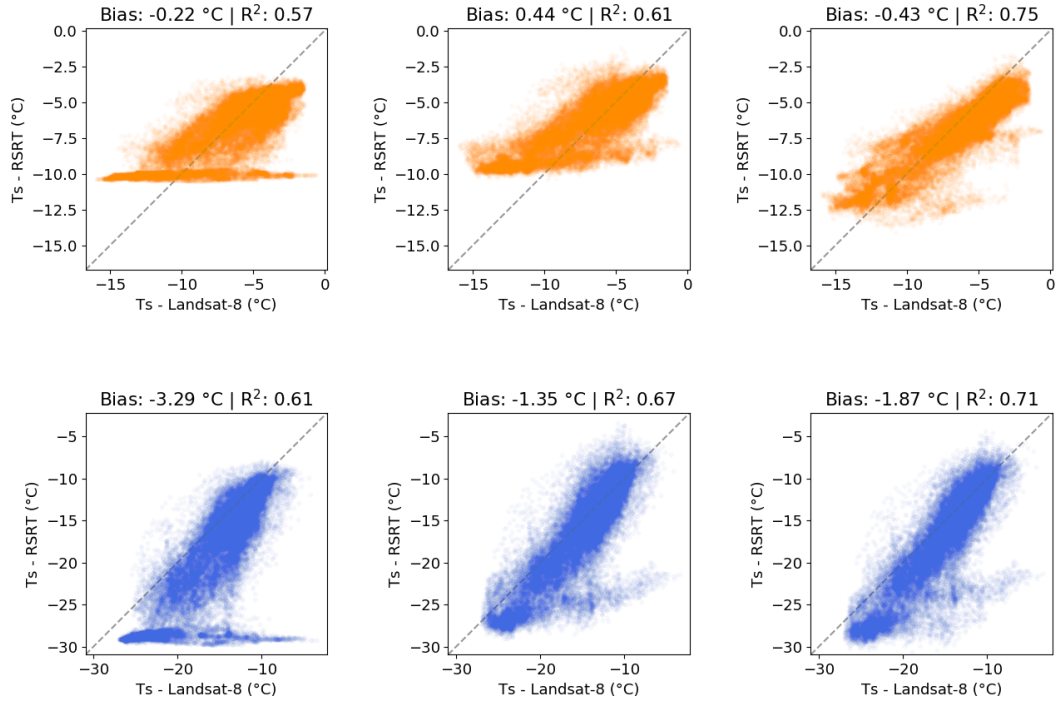
FIGURE 12 – Comparisons of simulated T_s by the model and observed T_s by Landsat-8. No re-illumination considered (left), re-illumination considered (center) and lapse rate in air temperature also considered (right). Simulations corresponding to 18 February 2018 (top) and 27 February 2018 (bottom).

4.1 Snow surface temperature estimation

The first question that arises is about the performance of the model to estimate the T_s and the spatial variations. The simulations show an overall agreement with observations, as seen in Section 3.3. First, the simulated fluxes to be considered on the surface energy budget and the temporal evolution of T_s are very well represented for a daily cycle (Section 3.3.1). The choice of SSA and z0 values when in-situ measurements are not available is critical. Spatio-temporal variations of SSA play a crucial role on the absorption by the snowpack, which could explain the differences between the simulated and observed net shortwave flux (Figure 7 (top)), as here the value has been kept constant for the whole time series. The roughness length controls the sensible and latent heat fluxes, so it shall also be carefully selected. Here, a standard value of 10^{-3} m is assumed, based on previous works (i.e. Brock et al., 2006) and a few tests with other values. The results show a much smaller bias to the in-situ measurements than the one from the satellite observations (Figure 8). Considering the high accuracy of surface temperature measurements at FluxAlp, this highlights the performance of the modelling chain to estimate T_s at this particular point. Re-illumination here is estimated to be around 10 to 20%, but the location of the instrumented site is relatively homogeneous and flat, so not particularly representative of complex terrain.

The spatial variations are also well represented, in particular when accounting for all topography

effects. The small-scale variations in the cold areas seem to be underestimated because of the dominating role of the shadow (Figure 9). The lack of direct radiation governs the surface temperature in some areas, such as the eastern (N-E to S-E) slopes covered by the shadow at the south of the scene, as shown in Figure 10. Opposed slopes show variations of surface temperature on the order of 5 to 10 °C in a few hundreds of meters. The re-illumination of the latter from surrounding terrain reduces these gradients in areas where diffuse illumination is important. The key role played by the processes involved in complex terrain is shown in Figure 11 and Figure 12. Accounting for the re-illumination warms the simulations, in particular the coldest facets that do not receive direct radiation. On the other hand, considering the lapse rate effect in air temperature cools the high-altitude areas of the modelled surface, since the air temperature was taken at the FluxAlp site. The result of combining both processes lead to an increased agreement of the simulations with the satellite observations. R^2 increases from 0.57 to 0.75 and from 0.61 to 0.71, for the scenes considered (18 and 27 February 2018). These results show the necessity of considering topography to well simulate the spatial variations of surface temperature. A further implementation by considering the spatial variations of wind speed and humidity would certainly improve the estimation of surface temperature. The results are similar on the other two dates where in-situ SSA measurements are available alongside Landsat-8 acquisitions. The R^2 coefficient is equal to: 0.67, and 0.69 (on 2 February 2018 and 22 March 2018), with SSA values of 47 and 32 m^2 kg^{-1}.

4.2 Limitations and further work

The methods implemented here to estimate surface temperature show some limitations. First, the measurements with the thermal camera are not entirely satisfactory. Being able to compensate for the internal temperature changes caused by external factors (heating, ventilation, etc) would lead to more accurate measurements and would certainly avoid the observed large fluctuations. This is normally performed by a shutter operation – closing and opening of the sensor. Also, this solution should reduce the vignetting effect seen on images, which turns out to be a known issue when UAV images are stitched together while creating an ortophoto (Goldman, 2010). Once this step is achieved, a second step involving an external shutter whose temperature is known should improve both accuracy and precision of the measurements. Without taking this into account, TIR cameras can only be used to measure surface temperature when alongside a validation instrument, such as infrared radiometers, that can serve as reference values to perform external calibration. This is realistic for a ground-based experiment, but is not for application on an UAV-based measurement protocol, as it can be difficult to perform such calibrations in an alpine terrain.

Considering satellite observations, the choice of the method for atmosphere correction is essential. The upcoming calibrated data from Landsat-8 that will be released by USGS in 2020 (Web 3, last access: 19 June 2020) will make it possible to consider again split-window algorithms as the stray light issue on

Band 11 will be *a priori* resolved. In this study, the whole scene has been considered as snow-covered, with an emissivity assumed to be equal to 1 and an albedo spectrum adapted to snow. However in alpine areas as the studied one, mountain ridges or even lack of snow on sun-facing slopes will require an emissivity mask, where each pixel would have a particular value. This is normally achieved by means of NDVI-based classifications (Li et al., 2013), but in mountainous areas in winter a simple snow mask would be enough to better determine albedo and emissivity over the whole scene. Nevertheless, recent works (i.e. He et al., 2019) show the complexity of retrieving surface temperature in mountainous areas, the extreme heterogeneity of the terrain being the main cause.

Accounting for the modelling chain, SSA and z0 values should be carefully chosen. For the sake of simplicity, these values have been kept constant when no in-situ measurements were available ($20 \, \mathrm{m^2 \, kg^{-1}}$ and $10^{-3} \, \mathrm{m}$, respectively). An alternative method would be to derive SSA from satellite observations, as in Kokhanovsky et al. (2019). The turbulent heat fluxes depend on wind speed as well as on roughness length z0. In complex terrain, the wind dynamics are influenced by the local topography, and when the geostrophic wind is weak, the so-called thermally driven winds develop as a consequence of the radiative cooling (warming) of the surface. They are down-slope – katabatic (up-slope – anabatic) during the night (day). The spatial variations of wind speed can be large in complex terrain, and therefore impact the surface temperature.

Another limitation is the single validation point available within the study area, which limits this evaluation. Ideally, at least three validation points would permit to better evaluate the model, in particular if they are located on different locations covering representative areas of the scene, such as shadowed areas at different altitude or with a different slope aspect. Figure 9 shows the large temperature contrasts between opposed slopes.

5   Conclusion

The RSRT model and the whole modelling chain has been evaluated against in-situ measurements and remote sensing observations to estimate the snow surface temperature in rugged terrain. The key radiative processes that take place in mountainous areas have been assessed and their role has been evaluated. A first method of validation relies on UAV-based thermal camera measurements. Further work is needed to better understand the uncertainties and to manage the constraints related to thermal imagery measurements. A single-channel algorithm for atmospheric correction has been implemented here in order to use Landsat-8 thermal acquisitions as validation for the spatial distribution of T_s. A total of 20 winter, cloudless images, acquired between February 2015 and December 2019 have been selected. Using one validation point (FluxAlp measurement station, in the French Alps), a cold bias of nearly $2\,°\mathrm{C}$ is observed, which is considered acceptable with respect to the assumptions made. This is coherent with difficulties noted by other authors, such as He et al. (2019).

The model has been evaluated both on its performance simulating temporal evolution and spatial variations of T_s. A 30 h long time series was simulated to assess the fluxes of the surface energy budget, in addition to the surface temperature. An overall agreement is obtained with the in-situ measurements. Besides, the bias observed at FluxAlp for the 20 scenes corresponding to Landsat-8 acquisitions is of only -0.2 °C, which highlights its potential to estimate surface temperature nearby well-instrumented areas. Spatial variations are also well represented, showing differences up to 5 to 10 °C in a few hundreds of meters. This is influenced by the aspect of the tilted terrain. Accounting for topography effects, such as re-illumination or lapse rate, ameliorates significantly the simulations. Alongside in-situ measurements of SSA, the determination coefficient with respect to Landsat-8 images varies from $R^2 = 0.67$ to $R^2 = 0.75$. The model shows some limitations when SSA and z0 values are not available, so they should be carefully determined to estimate surface temperature.

The model shows performance to estimate the snow surface temperature and the spatial variations. It could be helpful to assess the requirements of future satellite missions as Trishna. This Franco-Indian programme will be focused in the thermal part of the spectrum, and the derived cryospheric applications could benefit from the understanding of the processes that govern the surface energy budget in snow-covered, mountainous areas.

References

Arnaud, L., Picard, G., Champollion, N., Domine, F., Gallet, J.-C., Lefebvre, E., Fily, M., and Barnola, J.-M.: Measurement of vertical profilesof snow specific surface area with a 1 cm resolution using infrared reflectance: instrument description and validation, J. Glaciol., 57, 17–29, https://doi.org/10.3189/002214311795306664, 2011.

Aubry-Wake, C., Baraer, M., McKenzie, J. M., Mark, B. G., Wigmore, O., Hellström, R. Å., Lautz, L., and Somers, L.: Measuring glacier surface temperatures with ground-based thermal infrared imaging, Geophys. Res. Lett., 42, 8489– 8497, https://doi.org/10.1002/2015GL065321, 2015.

Brenner, C., Thiem, C. E., Wizemann, H.-D., Bernhardt, M., and Schulz, K.: Estimating spatially distributed turbulent heat fuxes from high-resolution thermal imagery acquired with a UAV system, Int. J. Remote Sens., 38, 3003-3026, https://doi.org/10.1080/01431161.1280202, 2017.

Brock, B., Willis, I., and Sharp, M.: Measurement and parameterization of aerodynamic roughness length variations at Haut Glacier d'Arolla, Switzerland, J. Glaciol., 52(177), 281-297, https://doi.org/10.3189/172756506781828746, 2016.

Budzier, H. and Gerlach, G.: Calibration of uncooled thermal infrared cameras, J. Sens. Sens. Syst., 4, 187–197, https://doi.org/10.5194/jsss-4-187-2015, 2015.

Bühler, Y., Adams, M., Bösch, R., and Stoffel, A.: Mapping snow depth in alpine terrain with unmanned aerial systems (UASs): Potential and limitations, The Cryosphere, 10, 1075-1088, https://doi.org/10.5194/tc-10-1075-2016, 2016.

Campagnolo, M. L., Sun, Q., Liu, Y., Schaaf, C., Wang, Z., and Román, M. O.: Estimating the effective spatial resolution of theoperational BRDF, albedo, and nadir reflectance products from MODIS and VIIRS, Remote Sens. Environ., 175, 52–64, https://doi.org/10.1016/J.RSE.2015.12.033, 2016.

Carmagnola, C. M., Domine, F., Dumont, M., Wright, P., Strellis, B., Bergin, M., Dibb, J., Picard, G., Libois, Q., Arnaud, L., and Morin, S.: Snow spectral albedo at Summit, Greenland: measurements and numerical simulations based on physical and chemical properties of the snowpack, The Cryosphere, 7, 1139-1160, https://doi.org/10.5194/tc-7-1139-2013, 2013.

Choler, P., Laurent, J. P., Cohard, J-M., Biron, R., Delbart, F., and Aubert, S.: FLUXALP: un projet de développement d'une station de mesures éco-climatiques au col du Lautaret, Hautes-Alpes, France in: Actes du 27e colloque de l'Association Internationale de Climatologie, Dijon, France, 2-5 July 2014, 2014.

Copernicus Climate Change Service (C3S): ERA5: Fifth generation of ECMWF atmospheric reanalyses of the global climate. Copernicus Climate Change Service Climate Data Store (CDS), last access: 9 June 2020, 2017.

Cristóbal, J., Jiménez-Muñoz, J.C., Prakash, A., Mattar, C., Skoković, D., and Sobrino, J.A.: An improved single-channel method to retrieve land surface temperature from the Landsat-8 thermal band, Remote Sens., 10(3), 431, https://doi.org/10.3390/rs10030431 2018.

Dozier, J., Green, R. O., Nolin, A. W., and Painter, T. H.: Interpretation of snow properties from imaging spectrometry, Remote Sens. Environ., 113(1), S25 - S37, https://doi.org/10.1016/j.rse.2007.07.029, 2009.

Dumont, M., Arnaud, L., Picard, G., Libois, Q., Lejeune, Y., Nabat, P., Voisin, D., and Morin, S.: In situ continuous visible and near-infrared spectroscopy of an alpine snowpack, The Cryosphere, 11, 1091–1110, https://doi.org/10.5194/tc-11-1091-2017, 2017.

Essery, R., and Etchevers, P.: Parameter sensitivity in simulations of snowmelt, J. Geophys. Res., 109, D20111, https://doi.org/10.1029/2004JD005036, 2004.

Flanner, M. G., and Zender, C. S.: Snowpack radiative heating: Influence on Tibetan Plateau climate, Geophys. Res. Lett., 32, L06501, https://doi.org/10.1029/2004GL022076, 2005.

Flanner, M. G., Zender, C. S., Randerson, J. T., and Rasch, P. J.: Present-day climate forcing and response from black carbon in snow, J. Geophys. Res., 112, D11202, https://doi.org/10.1029/2006JD008003, 2007.

Gallet, J.-C., Domine, F., Zender, C. S., and Picard, G.: Measurement of the specific surface area of snow using infrared reflectance in an integrating sphere at 1310 and 1550 nm, The Cryosphere, 3, 167 – 182, https://doi.org/10.5194/tc-3-167-2009, 2009.

Goldman, D. B.: Vignette and exposure calibration and compensation, IEEE T. Pattern Anal., 32 (12), 2276-2288, https://doi.org/10.1109/TPAMI.2010.55, 2010..

Gómez-Candón, D., Virlet, N., Labbé, S., Jolivot, A. and Regnard, J. L.: Field phenotyping of water stress at tree scale by UAV-sensed imagery: new insights for thermal acquisition and calibration, Precis. Agric., 17, 786–800, https://doi.org/10.1007/s11119-016-9449-6, 2016.

Grenfell, T. and Warren, S.: Representation of a nonspherical ice particle by a collection of independent spheres for scattering and absorption of radiation, J. Geophys. Res., 104, 31697–31709, https://doi.org/10.1029/2000JC000414, 1999.

He, J., Zhao, W., Li, A., Wen, F., and Yu, D.: The impact of the terrain effect on land surface temperature variation based on Landsat-8 observations in mountainous areas, Int. J. Remote Sens., 40, 1808-1827, https://doi.org/10.1080/01431161.2018.1466082, 2019.

Imbrie J. and Imbrie J. Z.: Modeling the climatic response to orbital variations, Science, 207, 943–953, https://doi.org/10.1126/science.207.4434.943, 1980.

Jiménez-Muñoz, J. C., and Sobrino, J. A.: A generalized single-channel method for retrieving land surface temperature from remote sensing data, J. Geophys. Res., 108(D22), 4688, https://doi.org/10.1029/2003JD003480, 2003.

Jin, M., Li, J., Wang, C., and Shang, R. A practical split-window algorithm for retrieving land surface temperature from landsat-8 data and a case study of an urban area in China, Remote Sens, 7(4), 4371–4390, https://doi.org/10.3390/rs70404371, 2015.

Kokhanovsky, A. A., and Zege, E. P.: Scattering optics of snow, Appl. Opt., 43, 1589-1602, https://doi.org/10.1364/AO.43.001589, 2004.

Kokhanovsky, A., Lamare, M., Danne, O., Brockmann, C., Dumont, M., Picard, G., Arnaud, L., Favier, V., Jourdain, B., Le Meur, E., Di Mauro, B., Aoki, T., Niwano, M., Rozanov, V., Korkin, S., Kipfstuhl, S., Freitag, J., Hoerhold, M., Zuhr, A., Vladimirova, D., Faber, A.-K., Steen-Larsen, H.C., Wahl, S., Andersen, J.K., Vandecrux, B., van As, D., Mankoff, K.D., Kern, M., Zege, E., and Box, J.E.: Retrieval of snow properties from the Sentinel-3 Ocean and Land Colour Instrument, Remote Sens., 11, 2280, https://doi.org/10.3390/rs11192280, 2019.

Kraaijenbrink, P. D. A., Shea, J. M., Litt, M., Steiner, J. F., Treichler, D., Koch, I., and Immerzeel, W.W.: Mapping surface temperatures on a debris-covered glacier with an unmanned aerial vehicle, Front. Earth Sci., 6 (64), https://doi.org/10.3389/feart.2018.00064, 2018.

Lamare, M., Dumont, M., Picard, G., Larue, F., Tuzet, F., Delcourt, C., and Arnaud, L.: Simulating Optical Top-Of-Atmosphere Radiance Satellite Images over Snow-Covered Rugged Terrain, The Cryosphere Discuss., https://doi.org/10.5194/tc-2020-104, in review, 2020.

Larue, F., Picard, G., Arnaud, L., Ollivier, I., Delcourt, C., Lamare, M., Tuzet, F., Revuelto, J., and Dumont, M.: Snow albedo sensitivity to macroscopic surface roughness using a new ray-tracing model, The Cryosphere, 14, 1651–1672, https://doi.org/10.5194/tc-14-1651-2020, 2020.

Lee, W., Liou, K.N., and Wang, C.: Impact of 3-D topography on surface radiation budget over the Tibetan Plateau, Theor. Appl. Climatol., 113, 95–103, https://doi.org/10.1007/s00704-012-0767-y, 2013.

Leng, P., Song, X., Duan, S-B., and Li, Z-L.: A practical algorithm for estimating surface soil moisture using combined optical and thermal infrared data, Int. J. Appl. Earth Obs., 52, 338-348, https://doi.org/10.1016/j.jag.2016.07.004, 2016.

Lhermitte, S., Abermann, J., and Kinnard, C.: Albedo over rough snow and ice surfaces, The Cryosphere, 8, 1069–1086, https://doi.org/10.5194/tc-8-1069-2014, 2014.

Li, Z-L., Tang, B-H., Wu, H., Ren, H., Yan, G., Wan, Z., Trigo, I. F., and Sobrino, J. A.: Satellite-derived land surface temperature: Current status and perspectives, Remote Sens. Environ., 131, 14-37, https://doi.org/10.1016/j.rse.2012.12.008, 2013.

Male, D. H., and Granger, R. J.: Snow surface energy exchange, Water Resour. Res., 17(3), 609– 627, https://doi.org/10.1029/WR017i003p00609, 1981.

Marks, D., and Dozier, J.: A clear-sky longwave radiation model for remote alpine areas. Arch. Meteor. Geophy. B, 27, 159–187, https://doi.org/10.1007/BF02243741, 1979.

Mattar, C., Duran-Alarcon, C., Jimenez-Munoz, J.C., Santamaria-Artigas, A., Olivera-Guerra, L. and Sobrino, J.A.: Global atmospheric profiles from reanalysis information (GAPRI): A new database for earth surface temperature retrieval, Int. J. Remote Sens, 36, 5045–5060, https://doi.org/10.1080/01431161.2015.1054965, 2015.

Mondet, J. and Fily, M.: The reflectance of rough snow surfaces in Antarctica from POLDER/ADEOS remote sensing data, Geophys. Res. Lett., 26, 3477–3480, https://doi.org/10.1029/1999GL010913, 1999.

Montanaro, M., Gerace, A., Lunsford, A., and Reuter, D.: Stray light artifacts in imagery from the Landsat 8 Thermal Infrared Sensor. Remote Sens., 6(11), 10435-10456, https://doi.org/10.3390/rs61110435, 2014.

Pal Arya, S. (Ed.): Energy budget near the surface, in: Introduction to micrometeorology, International Geophysics (42), Academic Press, 9-20, https://doi.org/10.1016/S0074-6142(08)60417-9, 1988.

Picard, G.: A library to compute spectral albedo and extinction of snow, and correct albedo measurements from slope distortion (Version tc-paper), Zenodo, https://doi.org/10.5281/zenodo.3742138, 2020.

Picard, G., Brucker, L., Fily, M., Gallée, H., and Krinner, G.: Modeling timeseries of microwave brightness temperature in Antarctica. Journal of Glaciology, 55 (191), 537-551, https://doi.org/10.3189/002214309788816678, 2009.

Plüss, C. and Ohmura, A.: Longwave radiation on snow-covered mountainous surfaces. J. Appl. Meteor., 36, 818–824, https://doi.org/10.1175/1520-0450-36.6.818, 1997.

Ricchiazzi, P., Yang, S., Gautier, C., and Sowle, D.: SBDART: A research and teaching software tool for plane-parallel radiative transfer in the Earth's atmosphere. Bull. Amer. Meteor. Soc., 79, 2101–2114, https://doi.org/10.1175/1520-0477(1998)079<2101:SARATS>2.0.CO;2, 1998.

Rossini, M., Di Mauro, B., Garzonio, R., Baccolo, G., Cavallini, G., Mattavelli, M., De Amicis, M. and Colombo, R.: Rapid melting dynamics of an alpine glacier with repeated UAV photogrammetry, Geomorphology, 304, 159-172, https://doi.org/10.1016/j.geomorph.2017.12.039, 2018.

Sandmeier, S. and Itten, K.: A physically-based model to correct atmospheric and illumination effects in optical satellite data of ruggedterrain, IEEE T. Geosci. Remote, 35, 708–717, https://doi.org/10.1109/36.581991, 1997.

Skiles, S. M., Flanner, M., Cook, J. M., Dumont, M., and Painter,T. H.: Radiative forcing by light-absorbing particles in snow, Nat. Clim. Change, 8, 964–971, https://doi.org/10.1038/s41558-018-0296-5, 2018.

Tardy, B., Rivalland, V., Huc, M., Hagolle, O., Marcq, S., and Boulet, G.: A software tool for atmospheric correction and surface temperature estimation of landsat infrared thermal data, Remote Sens., 8(9), 696, https://doi.org/10.3390/rs8090696, 2016.

Tuzet, F., Dumont, M., Lafaysse, M., Picard, G., Arnaud, L., Voisin, D., Lejeune, Y., Charrois, L., Nabat, P., and Morin, S.: A multilayer physically based snowpack model simulating direct and indirect radiative impacts of light-absorbing impurities in snow, The Cryosphere, 11, 2633–2653,https://doi.org/10.5194/tc-11-2633-2017, 2017.

Tuzet, F., Dumont, M., Picard, G., Lamare, M., Voisin, D., Nabat, P., Lafaysse, M., Larue, F., Revuelto, J., and Arnaud, L.: Quantification of the radiative impact of light-absorbing particles during two contrasted snow seasons at Col du Lautaret (2058 m a.s.l., French Alps), The Cryosphere Discuss., https://doi.org/10.5194/tc-2019-287, in review, 2020.

Vionnet, V., Brun, E., Morin, S., Boone, A., Faroux, S., Le Moigne, P., Martin, E., and Willemet, J.-M.: The detailed snowpack scheme Crocus and its implementation in SURFEX v7.2, Geosci. Model Dev., 5, 773–791, https://doi.org/10.5194/gmd-5-773-2012, 2012.

Warren, S. G., Brandt, R. E., and O'Rawe Hinton, P.: Effect of surface roughness on bidirectional reflectance of Antarctic snow, J. Geophys. Res., 103(E11), 25789– 25807, https://doi.org/10.1029/98JE01898, 1998.

Web 1: Landsat Collection 2: https://www.usgs.gov/land-resources/nli/landsat/landsat-collection-2?qt-science_support_page_related_con=1#qt-science_support_page_related_con, last access: 19 June 2020.

Web 2: Géoportail: https://geoservices.ign.fr/documentation/index.html, last access: 19 June 2020.

Web 3: Landsat 8 OLI and TIRS Calibration Notices: https://www.usgs.gov/land-resources/nli/landsat/landsat-8-oli-and-tirs-calibration-notices, last access: 19 June 2020.

Web 4: Using the USGS Landsat Level-1 Data Product: https://www.usgs.gov/land-resources/nli/landsat/using-usgs-landsat-level-1-data-product, last access: 19 June 2020.

Web 5: IR120: Temperature Sensor specifications: https://www.campbellsci.eu/ir120, last access: 19 June 2020.

Appendix A   List of selected Landsat-8 scenes

Date	Path / Row	Product name
10 February 2015	196 / 029	LC08_L1TP_196029_20150210_20170413_01_T1
19 February 2015	195 / 029	LC08_L1TP_195029_20150219_20170412_01_T1
26 February 2015	196 / 029	LC08_L1TP_196029_20150226_20170412_01_T1
21 January 2016	195 / 029	LC08_L1TP_195029_20160121_20170405_01_T1
9 March 2016	195 / 029	LC08_L1TP_195029_20160309_20170328_01_T1
13 December 2016	196 / 029	LC08_L1TP_196029_20161213_20170316_01_T1
1 January 2018	196 / 029	LC08_L1TP_196029_20180101_20180104_01_T1
2 February 2018	196 / 029	LC08_L1TP_196029_20180202_20180220_01_T1
18 February 2018	196 / 029	LC08_L1TP_196029_20180218_20180307_01_T1
27 February 2018	195 / 029	LC08_L1TP_195029_20180227_20180308_01_T1
22 March 2018	196 / 029	LC08_L1TP_196029_20180322_20180403_01_T1
4 January 2019	196 / 029	LC08_L1TP_196029_20190104_20190130_01_T1
29 January 2019	195 / 029	LC08_L1TP_195029_20190129_20190206_01_T1
5 February 2019	196 / 029	LC08_L1TP_196029_20190205_20190221_01_T1
14 February 2019	195 / 029	LC08_L1TP_195029_20190214_20190222_01_T1
21 February 2019	196 / 029	LC08_L1TP_196029_20190221_20190308_01_T1
18 March 2019	195 / 029	LC08_L1TP_195029_20190318_20190325_01_T1
25 March 2019	196 / 029	LC08_L1TP_196029_20190325_20190403_01_T1
6 December 2019	196 / 029	LC08_L1TP_196029_20191206_20191217_01_T1
31 December 2019	195 / 029	LC08_L1TP_195029_20191231_20200111_01_T1

TABLE 3 – List of selected scenes

Appendix B   Scatterplots of all estimations